Title

Metabolic imaging with hyperpolarized 13C pyruvate magnetic resonance imaging in patients with renal tumors—Initial experience

Journal

Cancer, 127(15)

ISSN

0008-543X

Authors

Tang, Shuyu
Meng, Maxwell V
Slater, James B
et al.

Publication Date

2021-08-01

DOI

10.1002/cncr.33554

Peer reviewed

HHS Public Access

Author manuscript

Cancer. Author manuscript; available in PMC 2021 November 03.

Published in final edited form as:

Cancer. 2021 August 01; 127(15): 2693–2704. doi:10.1002/cncr.33554.

Metabolic Imaging With Hyperpolarized ^{13}C Pyruvate Magnetic Resonance Imaging in Patients With Renal Tumors—Initial Experience

Shuyu Tang, PhD[1,2], **Maxwell V. Meng, MD**[3], **James B. Slater, RPh, PhD**[1], **Jeremy W. Gordon, PhD**[1], **Daniel B. Vigneron, PhD**[1,2], **Bradley A. Stohr, MD, PhD**[4], **Peder E. Z. Larson, PhD**[1,2], **Zhen Jane Wang, MD**[1]

[1]Department of Radiology and Biomedical Imaging, University of California–San Francisco, San Francisco, California;

[2]UC Berkeley-UCSF Graduate Program in Bioengineering, University of California, San Francisco and University of California, Berkeley, California;

[3]Department of Urology, University of California–San Francisco, San Francisco, California;

[4]Department of Pathology, University of California–San Francisco, San Francisco, California

Abstract

BACKGROUND: Optimal treatment selection for localized renal tumors is challenging because of their variable biologic behavior and limitations in the preoperative assessment of tumor aggressiveness. The authors investigated the emerging hyperpolarized (HP) ^{13}C magnetic resonance imaging (MRI) technique to noninvasively assess tumor lactate production, which is strongly associated with tumor aggressiveness.

METHODS: Eleven patients with renal tumors underwent HP ^{13}C pyruvate MRI before surgical resection. Tumor ^{13}C pyruvate and ^{13}C lactate images were acquired dynamically. Five patients underwent 2 scans on the same day to assess the intrapatient reproducibility of HP ^{13}C pyruvate MRI. Tumor metabolic data were compared with histopathology findings.

RESULTS: Eight patients had tumors with a sufficient metabolite signal-to-noise ratio for analysis; an insufficient tumor signal-to-noise ratio was noted in 2 patients, likely caused by poor tumor perfusion and, in 1 patient, because of technical errors. Of the 8 patients, 3 had high-grade

Corresponding Authors: Peder E. Z. Larson, PhD, Department of Radiology and Biomedical Imaging, University of California–San Francisco, 505 Parnassus Avenue, Room S-353, San Francisco, CA 94143 (peder.larson@ucsf.edu); Zhen Jane Wang, MD, Department of Radiology and Biomedical Imaging, University of California–San Francisco, 505 Parnassus Avenue, Room S-353, San Francisco, CA 94143 (zhen.wang@ucsf.edu).

Shuyu Tang's current address: HeartVista, Inc, Los Altos, California

The last 2 authors contributed equally to this work.

AUTHOR CONTRIBUTIONS

Shuyu Tang ran the experiments, performed data analysis, and wrote the article. **Maxwell V. Meng** designed the experiments, recruited patients, and reviewed the article. **James B. Slater** assisted in running the experiments and reviewed the article. **Jeremy W. Gordon** assisted in running the experiments and reviewed the article. **Daniel B. Vigneron** assisted in the experiment design and reviewed the article. **Bradley A. Stohr** performed pathology analysis and reviewed the article. **Peder E. Z. Larson** designed the experiments, assisted in running the experiments, assisted in data analysis, and wrote the article. **Zhen Jane Wang** designed the experiments, assisted in recruiting patients, assisted in data analysis, and wrote the article.

Additional supporting information may be found in the online version of this article.

clear cell renal cell carcinoma (ccRCC), 3 had low-grade ccRCC, and 2 had chromophobe RCC. There was a trend toward a higher lactate-to-pyruvate ratio in high-grade ccRCCs compared with low-grade ccRCCs. Both chromophobe RCCs had relatively high lactate-to-pyruvate ratios. Good reproducibility was noted across the 5 patients who underwent 2 HP ^{13}C pyruvate MRI scans on the same day.

CONCLUSIONS: The current results demonstrate the feasibility of HP ^{13}C pyruvate MRI for investigating the metabolic phenotype of localized renal tumors. The initial data indicate good reproducibility of metabolite measurements. In addition, the metabolic data indicate a trend toward differentiating low-grade and high-grade ccRCCs, the most common subtype of renal cancer.

LAY SUMMARY:

- Renal tumors are frequently discovered incidentally because of the increased use of medical imaging, but it is challenging to identify which aggressive tumors should be treated.
- A new metabolic imaging technique was applied to noninvasively predict renal tumor aggressiveness.
- The imaging results were compared with tumor samples taken during surgery and showed a trend toward differentiating between low-grade and high-grade clear cell renal cell carcinomas, which are the most common type of renal cancers.

Keywords

hyperpolarized ^{13}C; lactate; magnetic resonance imaging; molecular; pyruvate; renal cell carcinoma

INTRODUCTION

The increased use of medical imaging has led to a significant increase in the incidental detection of localized renal tumors.[1,2] Most of these are localized renal cell carcinomas (RCCs), which can vary widely in their biologic aggressiveness.[1,3] As such, the management options have evolved over time and now range from active surveillance to radical nephrectomy.[4] However, conventional imaging with computed tomography (CT) and magnetic resonance imaging (MRI)—the cornerstones of renal tumor characterization—cannot reliably differentiate low-grade, indolent RCCs, which are often amenable to active surveillance, from high-grade, aggressive RCCs, which may require timely surgery. In addition, many incidentally detected benign renal tumors, such as oncocytomas and lipid-poor angiomyolipomas, cannot be reliably differentiated from RCCs by conventional imaging. Renal tumor biopsy is invasive and also has several limitations: up to 20% of biopsies are nondiagnostic,[5,6] and there is frequent under-grading of RCC,[7,8] which is problematic for selecting between active surveillance versus definitive treatment. This diagnostic ambiguity has resulted in many benign tumors and indolent RCCs being treated with potentially unnecessary surgery, with attendant surgical risks, high cost, and increased risk of chronic kidney and cardiovascular disease.[9,10] Notably, increased RCC detection and treatment have not translated into a decrease in cancer-specific mortality.[1,2] For example, since the advent of cross-sectional imaging, the incidence of RCC has more than doubled

in the United States, and increased CT imaging has been associated with a higher incidence of nephrectomy,[2] yet the incidence of metastatic disease from RCC and its mortality have remained the same.[2] This suggests the overdiagnosis and overtreatment of indolent tumors.[1,2] Therefore, there is an unmet clinical need for additional noninvasive methods to improve the diagnosis and risk stratification of localized renal tumors to guide patient management.

RCC is known as a metabolic disease because of an array of metabolic perturbations from genetic alterations that drive these tumors.[11] In particular, the up-regulation of aerobic glycolysis with lactate production (the *Warburg effect*) is an adaptation of aggressive RCC that aids in survival, growth, and metastasis[12–14] and is a potential therapeutic target.[13,15] The lactate dehydrogenase A (LDHA) gene encodes the enzyme that catalyzes the conversion of pyruvate to lactate. Multiple studies of RCC tissues have demonstrated that tumor LDHA expression correlates with tumor grade and clinical stage, and high tumor LDHA expression is a strong independent predictor of tumor progression and poor patient survival.[16–18] Immunohistochemical staining of tumor tissues has also revealed significantly higher protein expression of LDHA in RCCs compared with that in benign renal tumors such as oncocytomas.[19] High expression of monocarboxylate transporter 4 (MCT4), a lactate exporter essential for maintaining high levels of glycolysis and lactate production,[20] is associated with more aggressive RCC.[21–23] An overexpression of MCT1, which mediates pyruvate transport into the cells for subsequent metabolism into lactate, has also been associated with a poor prognosis in patients with clear cell RCC.[23] These studies provide the rationale for metabolic imaging of lactate production as a noninvasive means to provide information on renal tumor aggressiveness.

Hyperpolarized (HP) ^{13}C MRI is an emerging molecular imaging method that allows for the rapid, noninvasive, pathway-specific interrogation of dynamic metabolic processes that were previously inaccessible by imaging. Hyperpolarization, achieved through the dynamic nuclear polarization technique,[24] provides unprecedented gains in sensitivity (>10,000-fold signal increase) for imaging ^{13}C-enriched biomolecules that are endogenous, nontoxic, and nonradioactive. ^{13}C pyruvate, an endogenous molecule, is the most widely studied HP probe to date given its position at a critical branch point of multiple pathways, including glycolysis, the tricarboxylic acid cycle, and amino acid biosynthesis. Multiple preclinical studies have shown the ability of HP ^{13}C pyruvate MRI to monitor the increased pyruvate-to-lactate conversion that occurs with aggressive cancers[25,26] and to provide a rapid assessment of treatment response.[27,28] A schematic of HP ^{13}C pyruvate MRI for interrogating tumor pyruvate-to-lactate conversion mediated by the relevant transporters and enzyme is provided in Figure 1. Importantly, it has been demonstrated multiple initial human studies that HP ^{13}C pyruvate MRI is safe and feasible, including studies in prostate, brain, and breast cancers.[29–33]

In the current study, we applied HP ^{13}C pyruvate MRI for investigating the metabolic phenotype of localized renal tumors in patients. We demonstrate the feasibility of this technique, acquiring dynamic images of pyruvate and lactate in renal tumors with sufficient resolution and signal-to-noise ratio (SNR), as well as the reproducibility of the normalized

tumor ^{13}C pyruvate and ^{13}C lactate signals. Our initial data also indicate a trend toward an increasing HP ^{13}C lactate-to-pyruvate ratio from low-grade to high-grade clear cell RCC.

MATERIALS AND METHODS

Patient Recruitment

Institutional Review Board approval was obtained for this prospective study (Clinicaltrials.gov identifier: NCT04258462). Between January 2019 and August 2020, 11 patients with localized renal tumors ≥2 cm in greatest dimension who were already scheduled for surgical resection were recruited. All HP ^{13}C pyruvate MRI studies were acquired within 8 weeks of surgical resection.

Preparation and Injection of ^{13}C Pyruvate

An Investigational New Drug approval (IND 140751) was obtained from the US Food and Drug Administration for the injection of HP ^{13}C pyruvate and MRI in patients with renal tumors. A 1.47-gram dose of Good Manufacturing Practices [1-^{13}C]pyruvate (ISOTEC Stable Isotope Division; Millipore-Sigma, Merck KGaA, Miamisburg, Ohio) mixed with 15 mM electron paramagnetic agent (EPA) (AH111501; GE Healthcare, Oslo, Norway) was polarized using a 5-T SPINlab polarizer (GE Research, Niskayuna, New York) before being rapidly dissolved with 130 °C water and passed through a filter that removed the EPA. The solution was then collected in a receiver vessel and neutralized with sodium hydroxide and Tris(hydroxymethyl) aminomethane buffer. The receive assembly, which accommodates quality-control processes, provided rapid measurements of pH, pyruvate, and EPA concentrations, polarization, and temperature. In parallel, the HP ^{13}C pyruvate solution was drawn into a syringe (Medrad Inc, Warrendale, Pennsylvania) through a 0.2-μm sterile filter (ZenPure, Manassas, Virginia) and transported into the scanner for injection. The integrity of this filter was tested in accordance with manufacturer specifications before injection. A 0.43-mL/kg dose of approximately 250 mM HP ^{13}C pyruvate was injected at a rate of 5 mL per second through an intravenous catheter placed in the antecubital vein, followed by a 20-mL saline flush. Five patients received 2 injections, from 20 to 60 minutes apart, on the same day to assess intrapatient reproducibility of HP ^{13}C pyruvate MRI.

HP ^{13}C Pyruvate MRI

^{13}C pyruvate and ^{13}C lactate images through the kidney and tumor were acquired dynamically using a metabolite-specific imaging sequence comprised of spectral-spatial excitation and multislice, 2-dimensional, spiral gradient echo (GRE) readouts,[34] with a Helmholz pair *clam-shell* transmit coil around the torso and an 8-channel receive array consisting of 2 paddles placed posterior to the kidneys.[35] For 4 patients, a metabolite-specific, balanced steady-state free precession (MS-bSSFP) sequence, which has been shown to provide approximately 2.5-fold increases in metabolite signal,[36] was used to acquire ^{13}C lactate images. ^{13}C alanine images were also acquired in 6 patients. Scan parameters were 1.5 cm in-plane resolution, 4-second temporal resolution, 21-mm slice thickness, a 20-degree flip angle for pyruvate, and a 30-degree flip angle for lactate and alanine. ^{13}C dynamic metabolite imaging acquisitions were triggered to automatically start 6 seconds after bolus arrival in the kidneys; this was achieved using a specialized,

autonomous scanning protocol implemented on the RT-Hawk platform (HeartVista Inc, Los Altos, California) that also included real-time frequency and B1+ calibrations.[34]

Image Reconstruction and Data Analysis

For all studies, gridding of k-space data for image reconstruction was performed using the Kaiser-Bessel gridding method[37] (http://web.stanford.edu/class/ee369c/mfiles/gridkb.m [accessed March 24, 2021]) with an oversampling factor of 1.4 and a kernel width of 4.5. The gridded k-space data were then inverse Fourier transformed to the reconstructed image. Multichannel data were combined by using pyruvate signals to approximate coil sensitivity maps.[38] Images were zero-filled by a factor of 2, and a 2-dimensional Fermi filter was applied to reduce ringing artifacts. Area under the curve (AUC) images were calculated by summing the complex data through time. The SNR was calculated as the signal magnitude divided by the standard deviation of the real part of the noise.

Tumor AUC values were normalized to mean AUC values of the adjacent normal kidney parenchyma for each metabolite (ie, pyruvate, lactate, and alanine). The lactate-to-pyruvate ratio and the alanine-to-pyruvate ratio were calculated using the normalized AUC signals. To mitigate the variability of RF power and receiver coil sensitivities across slices, region of interests of the tumor and normal kidneys were selected from the same or adjacent slices.

Histology

Renal tumor histology and subtypes as well as tumor grade were determined according to standard-of-care clinical practice after surgery. The Fuhrman nuclear grading system was used clinically for grading clear cell and papillary RCCs. Fuhrman grade was assigned based on the highest grade present within the tumor. Grades 1 and 2 were classified as low grade, and Fuhrman grades 3 and 4 were classified as high grade. Fuhrman grading is not used for chromophobe RCCs. Chromophobe RCCs were classified as high grade if they showed angiolymphatic invasion, microscopic necrosis, or sarcomatoid differentiation.

RESULTS

HP ^{13}C pyruvate MRI was successfully acquired in 10 of the 11 patients. The 1 unsuccessful case was because of technical errors. Two additional patients were excluded from further analysis because the tumors had an insufficient SNR, which we suspected was caused by poor perfusion (see Supporting Fig. 1). The final data set consisted of 8 patients, and the demographics of these patients are listed in Table 1. No adverse effects were observed when the patients were monitored during the injection and for 30 minutes after the injection of HP ^{13}C pyruvate.

The time from the start of injection to bolus arrival in the kidneys ranged from 15 to 28 seconds (see Supporting Fig. 2). The SNR summed over all time points in the tumors ranged from 19.0 to 211.0 (mean, 75.0) for pyruvate, 6.5 to 24.0 (mean, 13.0) for lactate, and 2.3 to 9.2 (mean, 4.2) for alanine when acquired using the GRE sequence (Table 2). The tumor SNR ranged from 9.4 to 59.0 (mean, 32.0) for lactate acquired with the MS-bSSFP sequence (Table 2). Real-time measured frequency offsets ranged from −20 to 30 hertz, and real-time measured power offsets ranged from −55% to 6% (see Supporting Fig. 3).

Table 3 lists the mean tumor pyruvate and lactate signals normalized to those of adjacent normal kidney parenchyma in the 5 patients who had 2 HP ^{13}C pyruvate MRI acquisitions on the same day. In 3 of these 5 patients, ^{13}C lactate imaging was acquired using both the GRE and MS-bSSFP sequences. Normalization of tumor signal to that of the normal adjacent renal parenchyma enables a comparison of the lactate signal between the 2 acquisitions with different MRI sequences. The difference in tumor signal between the 2 HP ^{13}C pyruvate MRI acquisitions was calculated as the absolute difference between 2 acquisitions divided by the mean of the 2 acquisitions (acquired with the GRE sequence and/or the MS-bSSFP sequence). Across these 5 patients, there was a mean difference of 8.6% and 3.2% between the first and second acquisition for the normalized tumor pyruvate and lactate signals, respectively (Table 3).

Tumor histopathology results are provided in Table 1. There were 6 clear cell RCCs and 2 chromophobe RCCs. Of the 6 clear cell RCCs, 3 were low-grade (Fuhrman grade 2) tumors, and 3 were high-grade (Fuhrman grade 3 or 4) tumors. Supporting Table 1 provides the estimated percentage within each tumor along with the respective Fuhrman grade as well as the overall Fuhrman grade for the clear cell RCCs. One of the 2 chromophobe RCCs showed microscopic necrosis, a histopathology feature associated with tumor aggressiveness and a poor clinical outcome.[39] Figure 2 shows representative AUC and dynamic images of ^{13}C pyruvate, ^{13}C lactate, and ^{13}C alanine for a high-grade clear cell RCC and demonstrates the visualization of metabolites across multiple slices and dynamic time points. Figures 3, 4, and 5 show the AUC images of ^{13}C pyruvate, ^{13}C lactate, and ^{13}C lactate-to-pyruvate ratios for high-grade clear cell RCCs, low-grade clear cell RCCs, and chromophobe RCCs, respectively, across the 8 patients. For each tumor, the mean and maximum tumor ^{13}C lactate-to-pyruvate ratios are summarized in Figure 6. The 3 high-grade clear cell RCCs have a variable pyruvate signal and an increased lactate signal compared with adjacent normal kidney parenchyma (Fig. 3). The 3 low-grade clear cell RCCs have a high pyruvate signal and a variable lactate signal compared with adjacent normal kidney parenchyma (Fig. 4). There is a trend toward higher pyruvate-to-lactate ratios in high-grade (grade 3 and 4) clear cell RCCs compared with low-grade (grade 2) clear cell RCCs (Fig. 6). The 2 chromophobe RCCs showed relatively isointense pyruvate signal and increased lactate signal compared with adjacent normal kidney parenchyma (Fig. 5). Both chromophobe RCCs had relatively high mean tumor lactate-to-pyruvate ratios, and the chromophobe RCC with microscopic necrosis (patient 3) had the highest lactate-to-pyruvate ratio (Fig. 6). Supporting Figure 4 shows extended field of views AUC images of both kidneys at the level of the tumors. The mean tumor alanine-to-pyruvate ratio was available in 6 of the 8 tumors (see Supporting Table 2); no clear trend in the alanine-to-pyruvate ratio was observed between the different tumor histologies and grades.

DISCUSSION

This study demonstrates the feasibility of HP ^{13}C pyruvate MRI for investigating renal tumor metabolism. Our data demonstrate a trend toward higher pyruvate-to-lactate ratios in high-grade clear cell RCCs compared with low-grade clear cell RCCs. Clear cell RCC is the most common RCC subtype, accounting for approximately 70% of all RCCs. Although clear cell RCCs are generally considered a more aggressive subtype, studies have indicated

that approximately 60% of T1a (tumor ≤4 cm) clear cell RCCs are low-grade tumors that do not grow or evolve quickly into high-grade, aggressive tumors, and these can safely undergo initial active surveillance rather than resection.[3,40] Therefore, a reliable, noninvasive way to grade these tumors would be desirable. Proteomic and metabolomic analyses of human clear cell RCC have demonstrated that lactate increases in a grade-dependent manner.[14] Our HP MRI data are in agreement with those prior analyses of ex vivo tissues and suggest that tumor metabolic phenotype observed by this imaging method has the potential to provide information on tumor grade to guide the selection of active surveillance for these tumors.

We observed that both chromophobe RCCs had relatively high mean tumor lactate-to-pyruvate ratios. Chromophobe RCC represents the third most common RCC subtype (5%). Chromophobe RCCs have unusual histopathology features with irregular nuclei, and Fuhrman grading is not used in their evaluation and is not thought to be predictive of clinical outcome.[41] Instead, histopathology features, including sarcomatoid change, tumor necrosis, and pathologic tumor stage, have been identified as independent predictors of aggressive chromophobe RCC.[9,42] Although a large majority of chromophobe RCCs have a favorable prognosis, a distinct subset of these patients with such adverse pathology features have aggressive tumors that progress to metastatic disease.[39,43] In our current study, 1 patient had a chromophobe RCC that exhibited histologic tumor necrosis, and it has been hypothesized that such tumor necrosis is caused by hypoxia from rapidly proliferating tumor out-growing the blood supply.[39] This patient had a high level of tumor lactate, which may be explained in part by the presence of tumor necrosis. Future studies with a larger number of chromophobe RCCs are needed to investigate their pyruvate metabolism with respect to pathologic features and to compare them with other subtypes of RCCs.

Although the lactate-to-pyruvate ratio is the most commonly used in HP ^{13}C pyruvate MRI studies to represent tumor metabolism, it can have potential confounders. For example, some renal tumors are highly vascular, and it is possible that a fraction of the pyruvate remains within the intravascular space rather than in the extravascular space, where it is accessible for cellular uptake and metabolism. Therefore, the lactate-to-pyruvate ratio can underestimate true tumor metabolism. In addition, for tumors with different vascularity, the differences in the vascular pyruvate signal may potentially influence the comparison of tumor metabolism when using the lactate-to-pyruvate ratio. Nonetheless, our initial data indicate a trend toward a higher pyruvate-to-lactate ratio in high-grade clear cell RCCs compared with low-grade clear cell RCCs, which is in agreement with prior tissue analyses. Given the commonly seen intratumoral heterogeneity in RCCs,[44] future studies are needed to investigate whether the mean or the maximum tumor lactate-to-pyruvate ratio is more predictive of tumor grade.

In our study, a sufficient metabolite SNR was obtained in both AUC and dynamic images for pyruvate and lactate at a resolution of 1.5 × 1.5 × 2.1 cm. Use of the metabolite-specific bSSFP sequence[36] enabled a 2.3-fold SNR improvement in lactate compared with the GRE sequence. The bSSFP sequence may be applied in future studies to other lower signal metabolites, such as alanine and bicarbonate, to improve their SNR. An optimal combination of data from multichannel arrays has also been shown to improve the SNR.[38] Another way to further gain SNR is shortening the sample transfer time from polarizer to patient.

Currently, 60 seconds is a typical delay time from dissolution to injection. If this number can be reduced to 30 seconds,[45] the SNR will be increased approximately by a factor of 1.9 for HP ^{13}C pyruvate studies, assuming a T1 (longitudinal relaxation time) of 47 seconds[46] for ^{13}C pyruvate at the earth's field. These strategies of improving the SNR can enable higher resolution imaging to minimize partial volume averaging between tumor and normal kidney parenchyma, which would be particularly beneficial for small renal tumors, as well as to improve the assessment of intratumoral heterogeneity that occurs commonly in RCCs.[44]

Because of the relatively short window available for HP ^{13}C pyruvate magnetic resonance (MR) scanning (approximately 1 minute) and irreversible signal decay, the scan needs to be fast, precise, and make efficient use of the available magnetization. Furthermore, calibrations of the B0 and B1/RF fields for ^{13}C MRI are extremely challenging because of the low natural abundance of endogenous ^{13}C in vivo. Studies have shown that inaccuracies in the timing and calibrations under typical clinical imaging setups and physiologic variations can lead to >50% error in the quantification of pyruvate metabolism.[47,48] Therefore, in the current study, we used a prototype autonomous scanning system[34] to perform localized measurements of the bolus timing and the B0 and B1+fields in real-time after HP ^{13}C pyruvate injection and to feedback this information into the scanning to enable metabolic imaging with reproducible timings and accurate field calibrations. This is expected to lead to more robust and reproducible metabolism quantifications.

Indeed, our initial data suggest relatively good reproducibility of HP ^{13}C pyruvate MRI in kidney tumors, with a mean difference of 8.6% and 3.2% between the first and second acquisition for the normalized tumor pyruvate and lactate signals, respectively. This reproducibility is comparable to standard uptake value measurements in oncologic fluorodeoxyglucose-positron emission tomography (FDG-PET) studies, which have an approximately 10% within-subject coefficient of variation.[49] In our study, the tumor ^{13}C signals were normalized to mean signals in the adjacent normal kidney tissue, and this normalization accounted for different polarization levels of the injected ^{13}C-pyruvate as well as MRI acquisition differences between the GRE and MS-bSSFP sequences. The variation in the acquisition was minimized by using the prototype autonomous scanning system with real-time calibrations, with the remaining variation expected to be caused by physiologic differences and/or inherent noise in the MRI acquisition. A study of patients with prostate cancer who underwent 2 HP ^{13}C pyruvate MRI scans on the same day also suggested relatively good reproducibility of the technique.[33] Future studies with larger patient cohorts are needed to fully evaluate the reproducibility of HP ^{13}C pyruvate MRI. Such information is critical for longitudinal investigation of tumor metabolism in the setting of both tumor surveillance and treatment response monitoring.

In a case report of a single patient who had clear cell RCC imaged with HP ^{13}C pyruvate MRI, Tran et al demonstrated that the technique can depict intratumoral metabolic heterogeneity.[50] The chemical shift imaging sequence used in that study allowed single-slice imaging with limited temporal resolution (every 20 seconds). In our study, the image acquisition methods used enabled rapid multislice and dynamic metabolic assessment of the tumor at a temporal resolution of 4 seconds, and tumors showed sufficient SNR over multiple dynamic time points. We observed both spatial and temporal metabolic

heterogeneity, especially in larger tumors in our series. Although we present the metabolic data as the sum of the signal over time (AUC) in this report, such dynamic data may be modeled to provide further information on renal tumor metabolism that could be clinically useful. The ability to noninvasively observe tumor metabolic heterogeneity may also help guide renal tumor biopsy and improve the accuracy of grading, which is currently limited with biopsy.[7,8]

HP ^{13}C pyruvate MRI was previously shown to be safe in multiple initial human studies.[29–33] Similarly, we did not observe any adverse events in our patients. In the context of renal tumors, HP ^{13}C pyruvate MRI has particular advantages over conventional ^{1}H MR spectroscopy. Because of the intratumoral lipid frequently present in RCCs, in particular clear cell RCCs, ^{1}H MR spectroscopy for lactate detection is challenging because of the overlapping lactate and lipid peaks. It also does not specifically detect metabolically active lactate. In addition, ^{1}H MR spectroscopy requires long acquisition time. HP ^{13}C pyruvate MRI, by comparison, allows the assessment of relevant metabolites without background signal, and the fast imaging techniques used in our study permit a dynamic metabolic assessment of the lactate dehydrogenase-catalyzed conversion to ^{13}C lactate. HP ^{13}C pyruvate MRI can also be readily integrated into the current state-of-the-art MRI examination using scanners with multinuclear capability, thus enabling multipara-metric imaging. Although FDG-PET is used widely in oncology, it has had limited success in the characterization of renal tumors, attributed in part to the low-to-moderate differential uptake of FDG in renal tumors.[51] Importantly, FDG-PET provides no information about glucose metabolism beyond import and phosphorylation, and it cannot assess downstream glycolytic metabolism. RCCs, especially those that are aggressive, have increased lactate production, as previously discussed,[16–18] and such a metabolic shift cannot be assessed using FDG-PET.

Our study has several limitations. First, the number of patients was small for this pilot study, which was focused on establishing the feasibility of interrogating renal tumor metabolism using HP ^{13}C pyruvate MRI. Therefore, larger cohort studies are being planned to fully investigate the utility of the technique for risk stratifying renal tumors. Second, the coil profile inhomogeneity across different locations in the imaged volume can potentially affect metabolism quantification. This effect is greatly reduced when using metabolite ratios because all metabolites experience the same profile. To minimize this effect when examining individual metabolites, we normalized tumor metabolism to adjacent normal kidney parenchyma metabolism and also acquired B1+ maps to measure transmit inhomogeneity. Because both the tumor and the adjacent normal kidney experience a similar coil profile inhomogeneity, using their ratios is expected to minimize such an effect. Third, the imaging resolution used in this first study may potentially lead to partial volume averaging for small renal tumors. For future studies, voxel shifting can be performed to achieve the maximum number of voxels that are entirely within the tumor. As discussed above, recent development in acquisition and coil combination strategies has enabled improved resolution.[36,38] Because HP ^{13}C MRI is rapidly improving, it is anticipated that a further improvement in resolution can be achieved for future studies. Fourth, we do not have tissue data on relevant enzymes and transporters involved in pyruvate metabolism, such as LDHA, MCT4, and MCT1, to correlate with imaging findings in this initial feasibility study. Such correlative studies are

planned for future studies to better understand the biologic underpinning of the HP ^{13}C MRI findings.

Conclusions

We have demonstrated the feasibility of HP ^{13}C pyruvate MRI for interrogating renal tumor metabolic phenotypes. Our initial data indicate that metabolite measurements have relatively good reproducibility, which is important for both tumor surveillance and treatment monitoring. In addition, the metabolic data in this pilot study indicate a trend toward differentiating between low-grade and high-grade clear cell RCCs, the most common subtype of renal cancer. The ability of this innovative metabolic imaging technology to distinguish among renal tumors of various histologies and grades will need to be further investigated in future studies to assess the full potential of HP ^{13}C MRI for risk stratifying renal tumors and for guiding patient clinical management.

Supplementary Material

Refer to Web version on PubMed Central for supplementary material.

FUNDING SUPPORT

This work was supported by the National Institutes of Health (P41EB013598 and U01EB026412) and by a Research Scholar Grant from the American Cancer Society (131715-RSG-18-005-01-CCE).

CONFLICT OF INTEREST DISCLOSURES

Shuyu Tang was a PhD student and postdoctoral student at the University of California-San Francisco and is currently an employee at HeartVista Inc. Peder E. Z. Larson reports grants from GE Healthcare and Myokardia Inc, grants and other support from Imaginostics, and personal fees from Human Longevity Inc, outside the submitted work. The remaining authors made no disclosures.

We thank the following individuals for their assistance with this study: Kimberly Okamoto, Mary Frost, Robert Bok, Namasvi Jariwala, Evelyn Escobar, Romelyn Delos Santos, Andrew Riselli, Priscilla Chan, Lucas Carvajal, Mark VanCriekinge, Philip Lee, Hsin-Yu Chen, Yaewon Kim, and Jasmine Graham.

REFERENCES

1. Hollingsworth JM, Miller DC, Daignault S, Hollenbeck BK. Rising incidence of small renal masses: a need to reassess treatment effect. J Natl Cancer Inst. 2006;98:1331–1334. [PubMed: 16985252]
2. Welch HG, Skinner JS, Schroeck FR, Zhou W, Black WC. Regional variation of computed tomographic imaging in the United States and the risk of nephrectomy. JAMA Intern Med. 2018;178:221–227. [PubMed: 29279887]
3. Rothman J, Egleston B, Wong YN, Iffrig K, Lebovitch S, Uzzo RG. Histopathological characteristics of localized renal cell carcinoma correlate with tumor size: a SEER analysis. J Urol. 2009;181:29–33; discussion 33–24. [PubMed: 19012902]
4. Campbell S, Uzzo R, Allaf ME, et al. Renal mass and localized renal cancer: AUA Guideline. J Urol. 2017;198:520–529. [PubMed: 28479239]
5. Leveridge MJ, Finelli A, Kachura JR, et al. Outcomes of small renal mass needle core biopsy, nondiagnostic percutaneous biopsy, and the role of repeat biopsy. Euro Urol. 2011;60:578–584.
6. Patel HD, Johnson MH, Pierorazio PM, et al. Diagnostic accuracy and risks of biopsy in the diagnosis of a renal mass suspicious for localized renal cell carcinoma: systematic review of the literature. J Urol. 2016;195:1340–1347. [PubMed: 26901507]
7. Harris CR, Whitson JM, Meng MV. Under-grading of <4 cm renal masses on renal biopsy. BJU Int. 2012;110:794–797. [PubMed: 22404857]

8. Bernhard JC, Bigot P, Pignot G, et al. The accuracy of renal tumor biopsy: analysis from a national prospective study. World J Urol. 2015;33:1205–1211. [PubMed: 25373933]
9. Clark MA, Shikanov S, Raman JD, et al. Chronic kidney disease before and after partial nephrectomy. J Urol. 2011;185:43–48. [PubMed: 21074205]
10. Kates M, Badalato GM, Pitman M, McKiernan JM. Increased risk of overall and cardiovascular mortality after radical nephrectomy for renal cell carcinoma 2 cm or less. J Urol. 2011;186:1247–1253. [PubMed: 21849201]
11. Rathmell WK, Rathmell JC, Linehan WM. Metabolic pathways in kidney cancer: current therapies and future directions. J Clin Oncol. 2018;36:3540–3546.
12. Linehan WM, Srinivasan R, Schmidt LS. The genetic basis of kidney cancer: a metabolic disease. Nat Rev Urol. 2010;7:277–285. [PubMed: 20448661]
13. van der Mijn JC, Panka DJ, Geissler AK, Verheul HM, Mier JW. Novel drugs that target the metabolic reprogramming in renal cell cancer. Cancer Metab. 2016;4:14. [PubMed: 27418963]
14. Wettersten HI, Hakimi AA, Morin D, et al. Grade-dependent metabolic reprogramming in kidney cancer revealed by combined proteomics and metabolomics analysis. Cancer Res. 2015;75:2541–2552. [PubMed: 25952651]
15. Sudarshan S, Karam JA, Brugarolas J, et al. Metabolism of kidney cancer: from the lab to clinical practice. Eur Urol. 2013;63:244–251. [PubMed: 23063455]
16. Girgis H, Masui O, White NM, et al. Lactate dehydrogenase A is a potential prognostic marker in clear cell renal cell carcinoma. Mol Cancer. 2014;13:101. [PubMed: 24885701]
17. Masui O, White NMA, DeSouza LV, et al. Quantitative proteomic analysis in metastatic renal cell carcinoma reveals a unique set of proteins with potential prognostic significance. Mol Cell Proteomics. 2013;12:132–144. [PubMed: 23082029]
18. White NMA, Newsted DW, Masui O, Romaschin AD, Siu KWM, Yousef GM. Identification and validation of dysregulated metabolic pathways in metastatic renal cell carcinoma. Tumour Biol. 2014;35:1833–1846. [PubMed: 24136743]
19. Singer K, Kastenberger M, Gottfried E, et al. Warburg phenotype in renal cell carcinoma: high expression of glucose-transporter 1 (GLUT-1) correlates with low CD8(+) T-cell infiltration in the tumor. Int J Cancer. 2011;128:2085–2095. [PubMed: 20607826]
20. Halestrap AP, Price NT. The proton-linked monocarboxylate transporter (MCT) family: structure, function and regulation. Biochem J. 1999;343(pt 2):281–299. [PubMed: 10510291]
21. Kim Y, Choi JW, Lee JH, Kim YS. Expression of lactate/H(+) symporters MCT1 and MCT4 and their chaperone CD147 predicts tumor progression in clear cell renal cell carcinoma: immunohistochemical and The Cancer Genome Atlas data analyses. Hum Pathol. 2015;46:104–112. [PubMed: 25456395]
22. Gerlinger M, Santos CR, Spencer-Dene B, et al. Genome-wide RNA interference analysis of renal carcinoma survival regulators identifies MCT4 as a Warburg effect metabolic target. J Pathol. 2012;227:146–156. [PubMed: 22362593]
23. Cao YW, Liu Y, Dong Z, et al. Monocarboxylate transporters MCT1 and MCT4 are independent prognostic biomarkers for the survival of patients with clear cell renal cell carcinoma and those receiving therapy targeting angiogenesis. Urol Oncol. 2018;36:311.e15–311.e25.
24. Ardenkjaer-Larsen JH, Fridlund B, Gram A, et al. Increase in signal-to-noise ratio of >10,000 times in liquid-state NMR. Proc Natl Acad Sci U S A. 2003;100:10158–10163. [PubMed: 12930897]
25. Keshari KR, Sriram R, Koelsch BL, et al. Hyperpolarized 13C-pyruvate magnetic resonance reveals rapid lactate export in metastatic renal cell carcinomas. Cancer Res. 2013;73:529–538. [PubMed: 23204238]
26. Albers MJ, Bok R, Chen AP, et al. Hyperpolarized 13C lactate, pyruvate, and alanine: noninvasive biomarkers for prostate cancer detection and grading. Cancer Res. 2008;68:8607–8615. [PubMed: 18922937]
27. Day SE, Kettunen MI, Gallagher FA, et al. Detecting tumor response to treatment using hyperpolarized 13C magnetic resonance imaging and spectroscopy. Nat Med. 2007;13:1382–1387. [PubMed: 17965722]

28. Saito K, Matsumoto S, Takakusagi Y, et al. 13C-MR spectroscopic imaging with hyperpolarized [1−13C]pyruvate detects early response to radiotherapy in SCC tumors and HT-29 tumors. Clin Cancer Res. 2015;21:5073–5081. [PubMed: 25673698]
29. Nelson SJ, Kurhanewicz J, Vigneron DB, et al. Metabolic imaging of patients with prostate cancer using hyperpolarized [1−13C]pyruvate. Sci Transl Med. 2013;5:198ra108.
30. Miloushev VZ, Granlund KL, Boltyanskiy R, et al. Metabolic imaging of the human brain with hyperpolarized (13)C pyruvate demonstrates (13)C lactate production in brain tumor patients. Cancer Res. 2018;78:3755–3760. [PubMed: 29769199]
31. Park I, Larson PEZ, Gordon JW, et al. Development of methods and feasibility of using hyperpolarized carbon-13 imaging data for evaluating brain metabolism in patient studies. Magn Reson Med. 2018;80:864–873. [PubMed: 29322616]
32. Gallagher FA, Woitek R, McLean MA, et al. Imaging breast cancer using hyperpolarized carbon-13 MRI. Proc Natl Acad Sci U S A. 2020;117:2092–2098. [PubMed: 31964840]
33. Granlund KL, Tee SS, Vargas HA, et al. Hyperpolarized MRI of human prostate cancer reveals increased lactate with tumor grade driven by monocarboxylate transporter 1. Cell Metab. 2020;31:105–114.e3. [PubMed: 31564440]
34. Tang S, Milshteyn E, Reed G, et al. A regional bolus tracking and real-time B1 calibration method for hyperpolarized (13)C MRI. Magn Reson Med. 2019;81:839–851. [PubMed: 30277268]
35. Tropp J, Lupo JM, Chen A, et al. Multi-channel metabolic imaging, with SENSE reconstruction, of hyperpolarized [1-(13)C]pyruvate in a live rat at 3.0 tesla on a clinical MR scanner. J Magn Reson. 2011;208:171–177. [PubMed: 21130012]
36. Tang S, Bok R, Qin H, et al. A metabolite-specific 3D stack-of-spiral bSSFP sequence for improved lactate imaging in hyperpolarized [1-(13) C]pyruvate studies on a 3T clinical scanner. Magn Reson Med. 2020;84:1113–1125. [PubMed: 32086845]
37. Jackson JI, Meyer CH, Nishimura DG, Macovski A. Selection of a convolution function for Fourier inversion using gridding [computerised tomography application]. IEEE Trans Med Imaging. 1991;10: 473–478. [PubMed: 18222850]
38. Zhu Z, Zhu X, Ohliger MA, et al. Coil combination methods for multi-channel hyperpolarized (13)C imaging data from human studies. J Magn Reson. 2019;301:73–79. [PubMed: 30851668]
39. Zini L, Leroy X, Lemaitre L, et al. Tumour necrosis in chromophobe renal cell carcinoma: clinical data to distinguish aggressive variants. Eur J Surg Oncol. 2008;34:687–691. [PubMed: 17997271]
40. Pierorazio PM, Hyams ES, Mullins JK, Allaf ME. Active surveillance for small renal masses. Rev Urol. 2012;14(1–2):13–19. [PubMed: 23172995]
41. Cheville JC, Lohse CM, Sukov WR, Thompson RH, Leibovich BC. Chromophobe renal cell carcinoma: the impact of tumor grade on outcome. Am J Surg Pathol. 2012;36:851–856. [PubMed: 22367296]
42. Volpe A, Novara G, Antonelli A, et al. Chromophobe renal cell carcinoma (RCC): oncological outcomes and prognostic factors in a large multicentre series. BJU Int. 2012;110:76–83. [PubMed: 22044519]
43. Amin MB, Paner GP, Alvarado-Cabrero I, et al. Chromophobe renal cell carcinoma: histomorphologic characteristics and evaluation of conventional pathologic prognostic parameters in 145 cases. Am J Surg Pathol. 2008;32:1822–1834. [PubMed: 18813125]
44. Gerlinger M, Rowan AJ, Horswell S, et al. Intratumor heterogeneity and branched evolution revealed by multiregion sequencing. N Engl J Med. 2012;366:883–892. [PubMed: 22397650]
45. Ardenkjaer-Larsen JH. Hyperpolarized MR—what's up doc? J Magn Reson. 2019;306:124–127. [PubMed: 31307893]
46. Chattergoon N, Martinez-Santiesteban F, Handler WB, Ardenkjaer-Larsen JH, Scholl TJ. Field dependence of T1 for hyperpolarized [1−13C]pyruvate. Contrast Media Mol Imaging. 2013;8:57–62. [PubMed: 23109393]
47. Durst M, Koellisch U, Gringeri C, et al. Bolus tracking for improved metabolic imaging of hyperpolarised compounds. J Magn Reson. 2014;243:40–46. [PubMed: 24717443]
48. Chen H, Larson P, Gordon JW, et al. Dynamic hyperpolarized 13C CS-EPSI of human prostate cancer—initial experience on 17 patients testing acquisition and quantitative analysis methods.

Paper presented at: International Society of Magnetic Resonance in Medicine—26th Annual Meeting; 4 14–20, 2018; Paris, France.

49. Lodge MA. Repeatability of SUV in oncologic (18)F-FDG PET. J Nucl Med. 2017;58:523–532. [PubMed: 28232605]
50. Tran M, Latifoltojar A, Neves JB, et al. First-in-human in vivo noninvasive assessment of intratumoral metabolic heterogeneity in renal cell carcinoma. BJR Case Rep. 2019;5:20190003. [PubMed: 31428445]
51. Ozcan A, Shen SS, Zhai QJ, Truong LD. Expression of GLUT1 in primary renal tumors: morphologic and biologic implications. Am J Clin Pathol. 2007;128:245–254. [PubMed: 17638658]

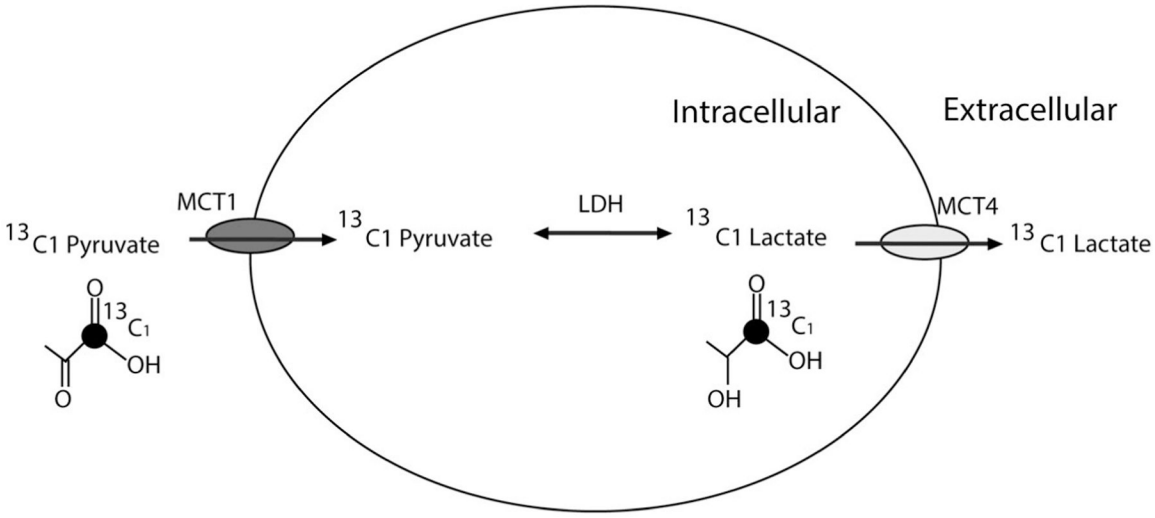

Figure 1.

This schematic illustrates the pyruvate-to-lactate metabolic pathway with relevant transporter and enzyme in renal tumors and the information that hyperpolarized ^{13}C pyruvate magnetic resonance imaging provides. LDH indicates lactate dehydrogenase; MCT, monocarboxylase transporter.

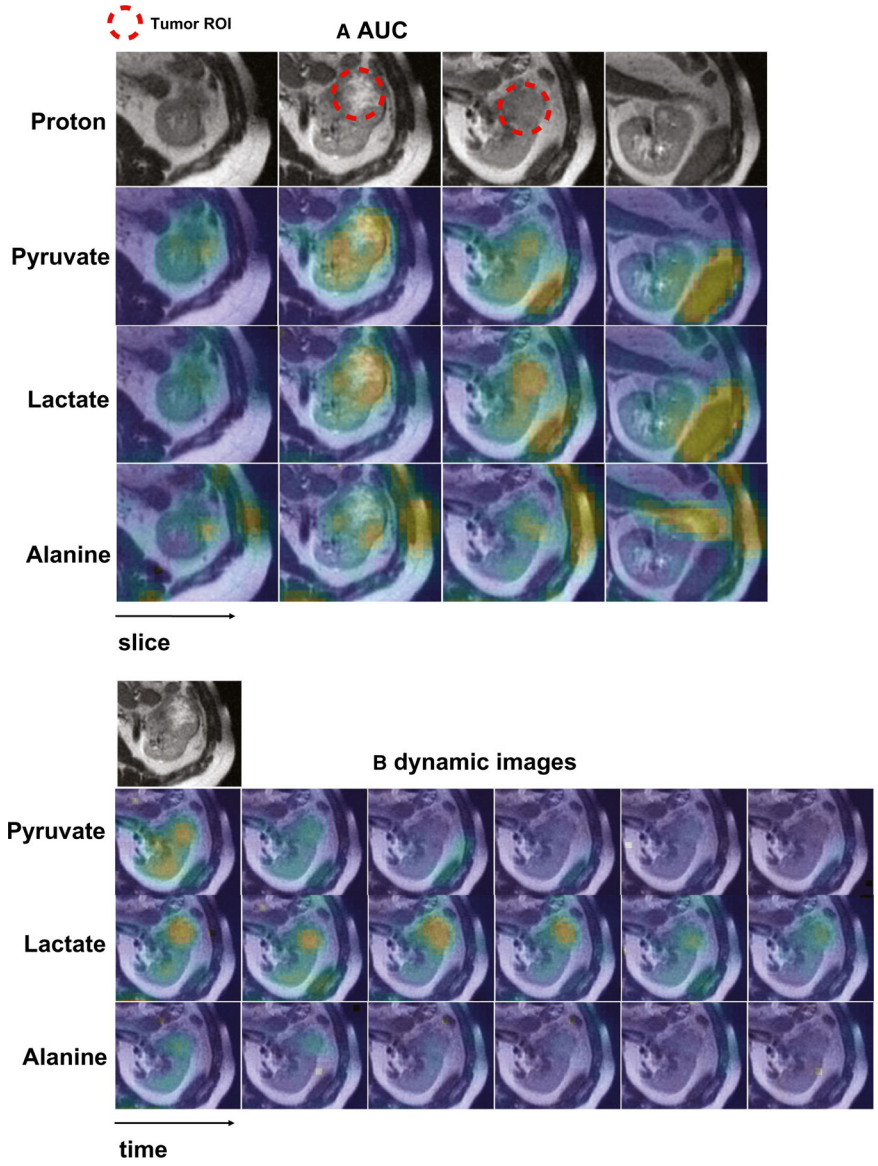

Figure 2.

Representative hyperpolarized ^{13}C pyruvate magnetic resonance images are shown from a man aged 41 years who had 5.8-cm, grade 4 renal cell carcinoma. (A) Area under the curve (AUC) and (B) dynamic images acquired every 4 seconds show a left kidney tumor with increased pyruvate, lactate, and alanine signals compared with adjacent normal parenchyma. The AUC images also show intratumoral metabolic heterogeneity. In the AUC images, the signal-to-noise-ratios of the tumor are 119 for pyruvate, 18 for lactate, and 5.2 for alanine. ROI indicates region of interest.

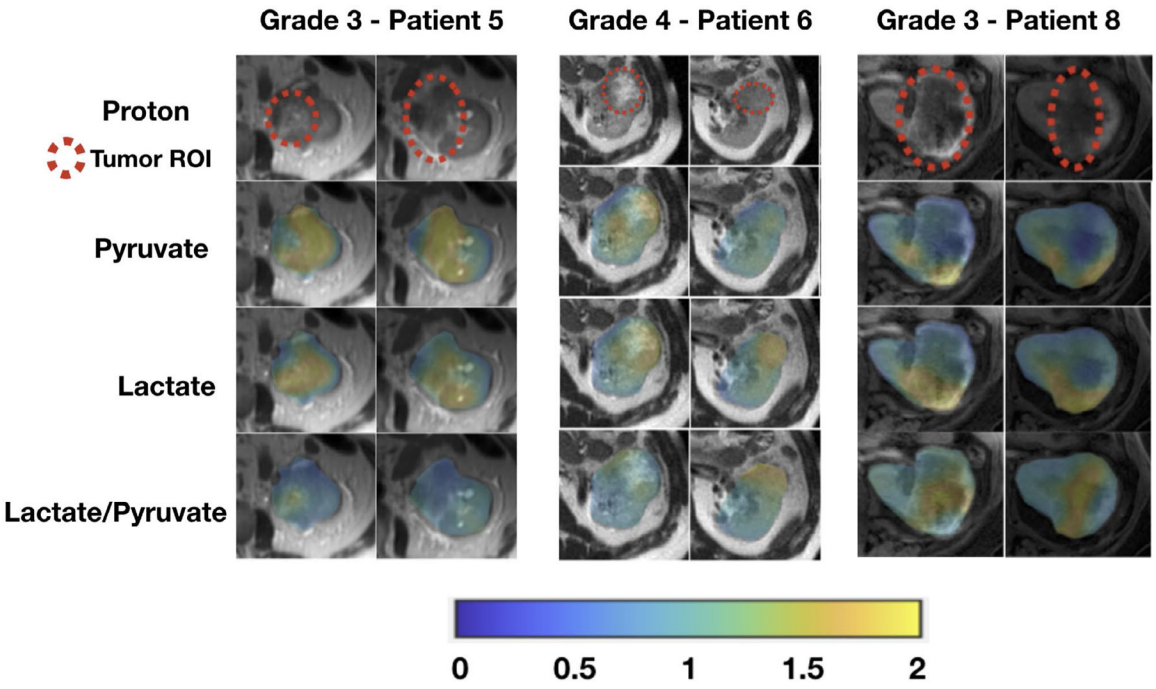

Figure 3.

These are area under the curve (AUC) images from hyperpolarized ^{13}C pyruvate magnetic resonance imaging of patients with high-grade (grade 3 and grade 4) clear cell renal cell carcinomas. Tumor AUC values were normalized to AUC values of the adjacent normal parenchyma for each metabolite. Lactate-to-pyruvate ratios were calculated using the normalized AUC signals. All images are displayed using the same color scale. ROI indicates region of interest.

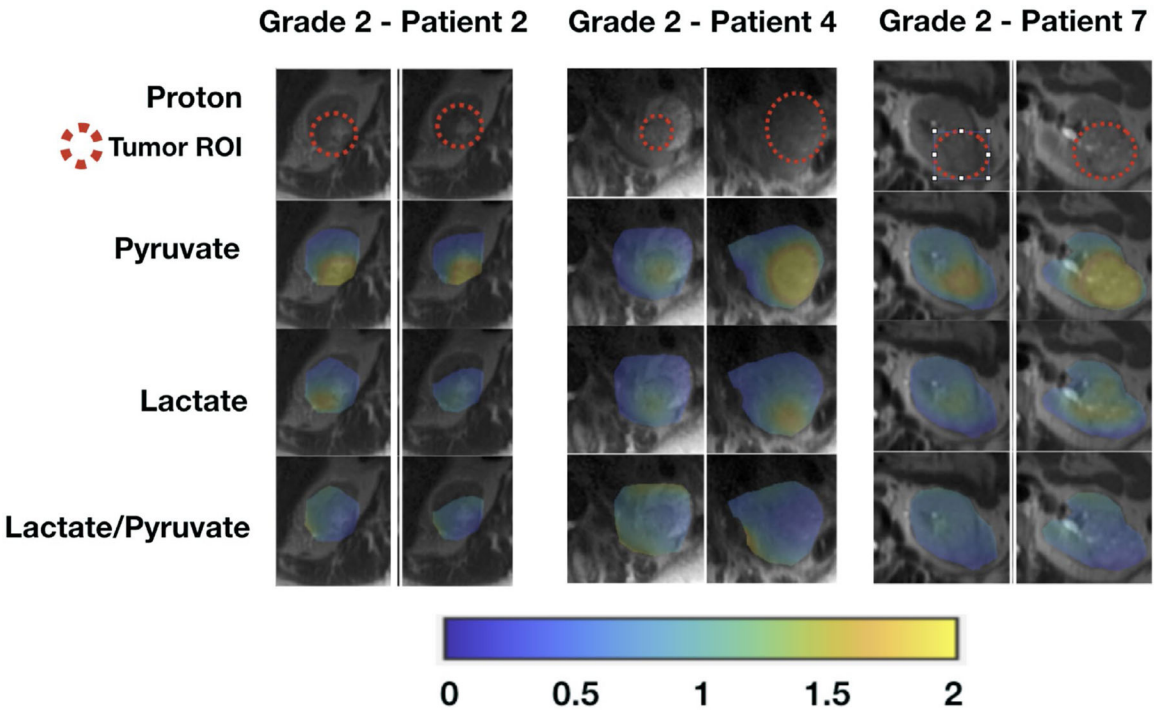

Figure 4.

These are area under the curve (AUC) images from hyperpolarized ^{13}C pyruvate magnetic resonance imaging of patients with low-grade (grade 2) clear cell renal cell carcinomas. Tumor AUC values were normalized to AUC values of the adjacent normal parenchyma for each metabolite. Lactate-to-pyruvate ratios were calculated using the normalized AUC signals. All images are displayed using the same color scale. ROI indicates region of interest.

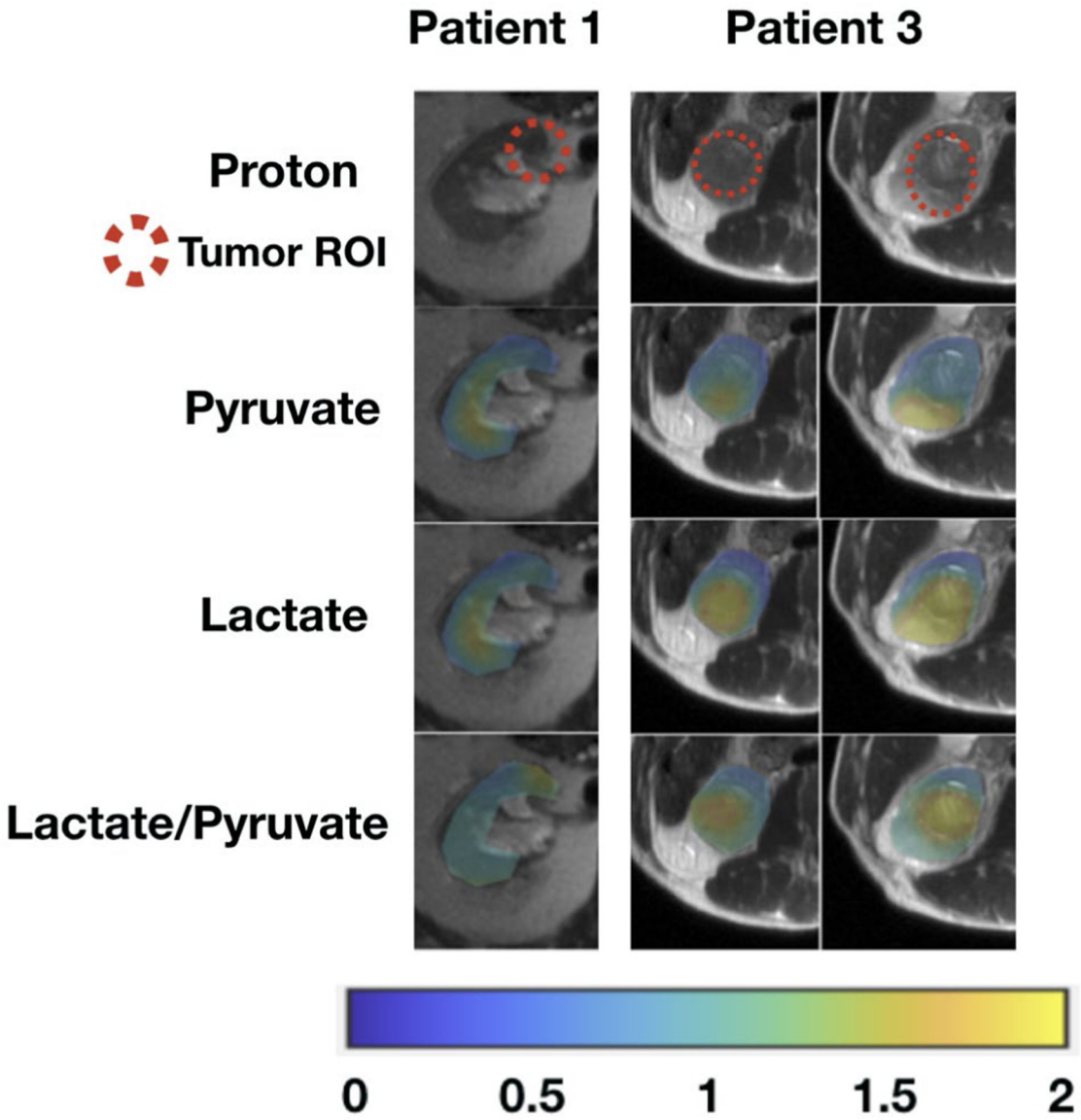

Figure 5.

These area under the curve (AUC) images from hyperpolarized ^{13}C pyruvate magnetic resonance imaging of patients with chromophobe renal cell carcinomas. Tumor AUC values were normalized to AUC values of the adjacent normal parenchyma for each metabolite. Lactate-to-pyruvate ratios were calculated using the normalized AUC signals. All images are displayed using the same color scale. ROI indicates region of interest.

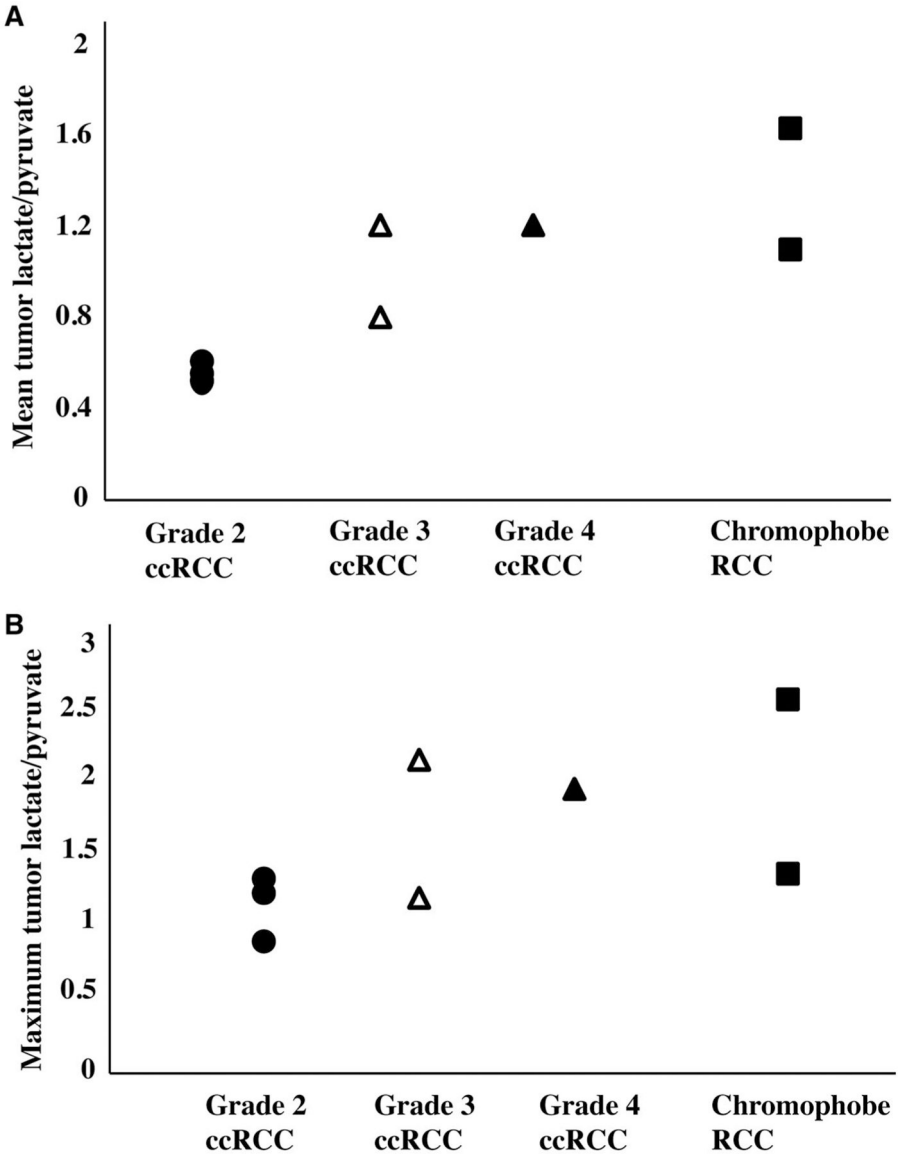

Figure 6.

The mean and maximum tumor lactate-to-pyruvate ratio is illustrated in 8 patients stratified by tumor histology and grade. The lactate-to-pyruvate ratios are the ratios between the normalized lactate area under the curve values and the normalized pyruvate area under the curve values, Charts depict (A) the mean tumor lactate-to-pyruvate ratio (mean of the lactate-to-pyruvate ratios when averaging all voxels for each tumor) and (B) the maximum lactate-to-pyruvate ratio for each tumor. There is a trend toward higher pyruvate-to-lactate ratio in high-grade (grade 3 and 4) clear cell renal cell carcinomas (ccRCCs) compared with low-grade (grade 2) ccRCCs. Both chromophobe RCCs demonstrate relatively high mean tumor lactate-to-pyruvate ratios; the chromophobe RCC with the highest lactate-to-pyruvate ratio also had a pathologic finding of microscopic necrosis, which has been associated with aggressive biology.

TABLE 1.

Patient Demographics, Renal Tumor Size and Histopathology

Patient	Age, y	Sex	Tumor Size, cm	Histology	Fuhrman Nuclear Grade	Other Pathology Findings	AJCC Tumor Classification	Anatomic stage
1	66	Man	2.5	Chromophobe	NA	Extension into perirenal fat	T3a	III
2	60	Man	3.5	Clear cell	2		T1a	I
3	80	Man	4.2	Chromophobe	NA	Tumor necrosis present	T1b	I
4	75	Woman	4.5	Clear cell	2	Extension into renal sinus fat	T3a	III
5	75	Man	6.5	Clear cell	3	Involving segmental renal vein	T3a	III
6	41	Man	5.8	Clear cell	4	Focal rhabdoid feature present; extension into segmental renal vein	T3a	III
7	37	Woman	4.9	Clear cell	2		T1b	I
8	78	Woman	7.0	Clear cell	3	Tumor necrosis and rhabdoid features present	T3a	III

Abbreviations: AJCC, American Joint Committee on Cancer; NA, not applicable (chromophobe renal cell carcinomas are not graded using the Fuhrman nuclear grading system).

TABLE 2.

Summary of Area Under the Curve Signal-to-Noise Ratios in Tumors

Patient	No. of Examinations	Pyruvate-GRE	Lactate-GRE	Lactate-bSSFP	Alanine-GRE
1	1	19	9.5	NA	NA
2	1	71	NA	9.4	4.1
3	1	37	NA	59	3.7
	2	34	24	NA	3.4
4	1	86	11	NA	4.5
	2	92	NA	23	4.4
5	1	62	8.7	NA	NA
	2	37	6.5	NA	NA
6	1	119	18	NA	5.2
	2	71	NA	38	2.7
7	1	211	18	NA	9.2
8	1	67	13	NA	2.3
	2	64	10	NA	2.6
Mean ± SD		75 ± 49	13 ± 5.8	32 ± 21	4.2 ± 2.0

Abbreviations: bSSFP, balanced steady-state free precession sequence; GRE, gradient echo sequence; NA, not available.

TABLE 3.

Comparison of Renal Tumor Area Under the Curve Signals Between 2 Hyperpolarized ^{13}C Pyruvate Magnetic Resonance Imaging Acquisitions in the Same Patient on the Same Day[a]

Patient	First Injection	Second Injection	Difference, %
Lactate			
3 (first bSSFP, second GRE)	1.59	1.30	20.0
4 (first GRE, second bSSFP)	0.96	0.97	1.0
5 (first GRE, second GRE)	1.45	1.38	5.1
6 (first GRE, second bSSFP)	1.24	1.41	12.6
8 (first GRE, second GRE)	0.78	0.75	4.0
Mean			8.6
Pyruvate			
3 (both GRE)	0.91	0.83	9.0
4 (both GRE)	1.72	1.72	0.3
5 (both GRE)	1.77	1.77	0.1
6 (both GRE)	1.08	1.11	2.3
8 (both GRE)	0.64	0.62	4.2
Mean			3.2

Abbreviations: bSSFP, balanced steady-state free precession sequence; GRE, gradient echo sequence.

[a]Tumor signals for each metabolite were normalized to adjacent mean kidney parenchyma signals. ^{13}C pyruvate images were acquired using GRE sequences. ^{13}C lactate images were acquired using either GRE or metabolite-specific bSSFP sequences.